High-Resolution Spectroscopy Used to Measure Inertial Confinement Fusion Neutron Spectra on OMEGA

Introduction

Nuclear diagnostics are essential to interpreting the condition of the DT fuel during compression in inertial confinement fusion (ICF) experiments.[1] Measurable parameters that determine the performance of ICF implosions include the ion temperature (T_i), areal density (ρR), and the primary DT neutron yield (Y_n) (Ref. 2). To achieve thermonuclear ignition, the alpha-particle heating must exceed the energy losses from the hot spot.[3] The DT fuel in the hot spot must have an areal density high enough to stop the alpha particles leaving the hot spot (typically >300 mg/cm^2), which boosts the core temperature into the ignition regime.[4]

A number of scaling laws have been developed where measurable parameters represent the progress toward fuel conditions necessary for ignition. The simplest of these laws depends on the T_i and ρR described by the 1-D parameter

$$\chi_{\text{1-D}} \approx \rho R^{0.8} \text{ g/cm}^2 \left(\frac{T_i}{4.4} \text{ keV} \right)^{1.8}, \qquad (1)$$

where $\chi_{\text{1-D}} > 1$ defines the ignition threshold.[5] A similar scaling law called ITFX, used on the National Ignition Facility (NIF), gives the probability of ignition as a function of experimental observables.[6,7]

A first approach to infer the areal density from cryogenic DT implosions was to measure the knock-on deuterons and tritons in the colder, dense shell, elastically scattered from the primary neutrons produced in the fusion reaction.[8,9] This technique has an increased uncertainty when the areal density approaches ~200 mg/cm^2 (Ref. 10). Advances in cryogenic implosions, such as using low-adiabat pulses and highly symmetric laser irradiation, have increased the areal density. The higher ρR results in a "leveling off" in the amount of knock-ons that leave the colder, dense shell as a result of the energy loss of the charged particles. An alternative method to infer the areal density in DT cryogenic implosions uses the primary neutrons that elastically scatter off the deuterons and tritons in the dense shell surrounding the hot spot.[1]

The magnetic recoil spectrometer (MRS) was one of the first methods to infer an areal density of >200 mg/cm^2 by measuring the forward-scattered neutron spectrum between 10 to 12 MeV (Ref. 11). This measurement is achieved by placing a plastic foil, either CH or CD, as close as possible to the DT implosion target. The neutrons from the reaction produce recoil protons (or deuterons) that are projected through a focusing magnet. The magnetic field deflects the recoiled protons (deuterons) onto an array of detectors according to their energy. This diagnostic has been successful for areal-density measurements on both OMEGA and the NIF.[12]

Neutron time-of-flight (nTOF) techniques have also been used to measure the areal density on the NIF using the elastically scattered neutron spectrum between 10 and 12 MeV (Ref. 13). These nTOF detectors use a liquid scintillation fluid with special properties to mitigate the long light-afterglow component.[14] Two identical detectors for two separate lines of sight have been calibrated on the OMEGA Laser System before installation on the NIF. The nTOF diagnostics have been successful in measuring the areal density on a large number of NIF cryogenic DT implosions and the results compare favorably with the MRS.
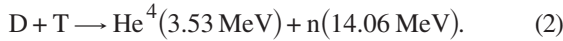
This article reports on a novel nTOF detector that was used for the first time to measure high-resolution, elastically scattered neutron spectra in the 1- to 6-MeV region on cryogenic DT implosions. A well-collimated, 13.4-m line of sight, designed with the aid of the Monte Carlo neutron transport code, and an nTOF detector with low-afterglow liquid scintillator compound were crucial to achieving a high-enough signal to background in the neutron spectrum at these energies. This new diagnostic is able to measure the areal density in the region from 50 to 250 mg/cm^2—typical values achieved in recent experiments where re-scattering of the scattered neutrons was negligible. Future experiments will result in higher areal densities (<1 g/cm^2). Less than 1% of the backscattered neutrons are being re-scattered even at these high areal densities, which will not reduce the accuracy of the areal-density measurements with this diagnostic. Multiple scattering becomes relevant only with areal densities well above 1 g/cm^2. Furthermore, simultane-

ous areal-density measurements from the MRS and the nTOF, which view the target from different directions, will allow for the study of asymmetric implosions on OMEGA.
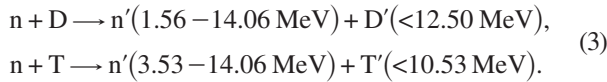
The ICF neutron energy spectrum of cryogenic DT implosions and the method used to infer the areal density from the elastically scattered neutrons will be described in the next section. The remaining sections will (1) describe the nTOF diagnostic design along with an improved shielded environment with a collimated line of sight that will minimize unwanted neutron scattering; (2) discuss the detector calibration method and the approach used to infer the areal density; and (3) present a summary and a short outlook on future work.

Inferring ρR from the ICF Neutron Energy Spectrum

The primary DT neutrons are generated from the fusion reaction[4]

$$D + T \longrightarrow He^4(3.53\,\text{MeV}) + n(14.06\,\text{MeV}). \quad (2)$$

A small fraction of the primary DT neutrons elastically scatter off the dense shell consisting of deuterons and tritons:

$$\begin{aligned} n + D &\longrightarrow n'(1.56 - 14.06\,\text{MeV}) + D'(<12.50\,\text{MeV}), \\ n + T &\longrightarrow n'(3.53 - 14.06\,\text{MeV}) + T'(<10.53\,\text{MeV}). \end{aligned} \quad (3)$$

Specifically, the number of down-scattered neutrons is given by

$$Y_{n'} = Y_n(r) \int_0^\infty \int_0^R (\sigma_d n_d + \sigma_t n_t)\,dr\,dt, \quad (4)$$

where $Y_n(r)$ is the quantity of 14.06-MeV neutrons at the radius r, σ_d and σ_t are the total elastic cross sections for the (n,d) and (n,t) interactions, with n_d and n_t the fuel ion density distributions. A simple derivation relates the areal density $\langle \rho R \rangle$ to the down-scattered neutrons' fraction[9]

$$\langle \rho R \rangle = 5 \frac{m_p}{(\sigma_d + \sigma_t)} \frac{Y_{n'}}{Y_n} \,\text{mg/cm}^2, \quad (5)$$
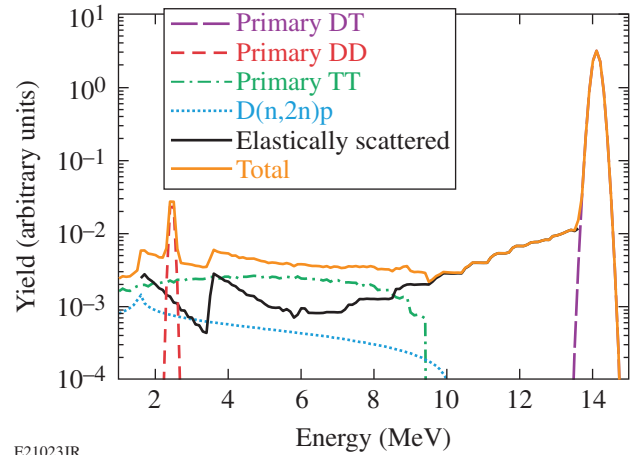
where m_p is the mass of the proton and σ_d and σ_t are the cross sections for neutron scattering off deuterium and tritium, respectively. The areal density is proportional to total down-scattered neutron fraction $Y_{n'}$ over the DT primary neutron yield Y_n. For average areal densities of <0.3 g/cm², typical for experiments on OMEGA, the primary neutrons typically experience no more than a single scatter event while leaving the compressed shell; double scattering is negligible. The kinematic

end point of these neutrons scattered from the dense DT shell is 3.53 MeV and 1.56 MeV, for scattering off the triton and deuteron, respectively, as calculated from[15]

$$\frac{E_{n'}}{E_n} = \frac{4A}{(1+A)^2}\cos^2\theta, \quad (6)$$

where $E_{n'}$ is the energy of the neutron after scattering, A is the atomic mass of the target nuclei (i.e., D to T), and θ is the recoil angle of the nucleus in the lab frame. The kinematic edge is defined by the value of $E_{n'}$ for $\theta = 0$, or the point at which maximum energy transfer occurs.

An example of the calculated neutron spectrum for a cryogenic DT implosion with an areal density of 220 mg/cm² and a T_i of 2.4 keV is shown in Fig. 131.23.

E21023JR

Figure 131.23
The neutron spectrum of a cryogenic DT implosion is generated from 1-D *LILAC* hydrodynamic simulations using the Monte Carlo postprocessor *IRIS*. This spectrum includes the primary DT peak (purple), DD peak (red), and TT neutron feature (green). A fraction (black) of the primary DT neutrons elastically scatter off the dense DT shell. The deuteron breakup reaction (light blue) becomes relevant below 2 MeV. These individual reactions result in the total neutron energy spectrum (orange).
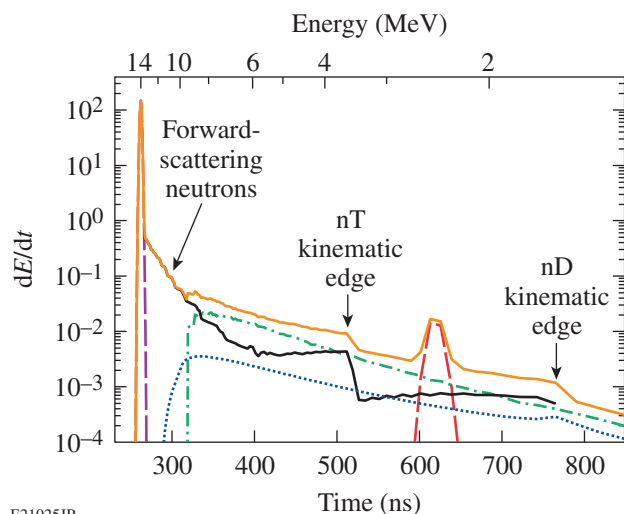
This spectrum was generated using 1-D *LILAC* simulations and post-processed in *IRIS*.[16] The largest contribution to the neutron spectrum comes from the primary D–T fusion reaction at 14.06 MeV. A second primary peak is the D–D fusion reaction at 2.45 MeV followed by the T–T fusion reaction, which is assumed isotropic, and shows a broad energy distribution with a range from 0 to 9.8 MeV (Ref. 17). The elastically scattered neutrons span the entire energy spectrum from 1 to 14.06 MeV.

The deuteron breakup, D(n,2n)p reaction, becomes important below 2 MeV.

The nD and nT elastic cross sections have been measured recently with high accuracy on OMEGA using DT-filled, thin-glass targets.[18] For DT cryogenic implosions, the backscattered neutrons probe the fuel assembly in the 1- to 6-MeV region (150° to 180°).

Setup of the Neutron Time-of-Flight Detector

A time-of-flight spectrum (Fig. 131.24) for a detector at 13.4 m from the target was generated from the neutron energy distribution discussed in the previous section.

Figure 131.24

A neutron time-of-flight spectrum generated for cryogenic DT implosions on OMEGA with a detector positioned 13.4 m from target chamber center. The primary DT peak (purple), primary DD peak (red), and TT spectrum (green) are generated by fusion reactions. The elastically scattered primary neutrons (black) extend ~10^5 down from the primary DT peak. Below 2 MeV (~700 ns) the deuteron breakup (blue) inelastic reaction becomes relevant. The total neutron spectrum (orange) is the combination of these individual contributions.
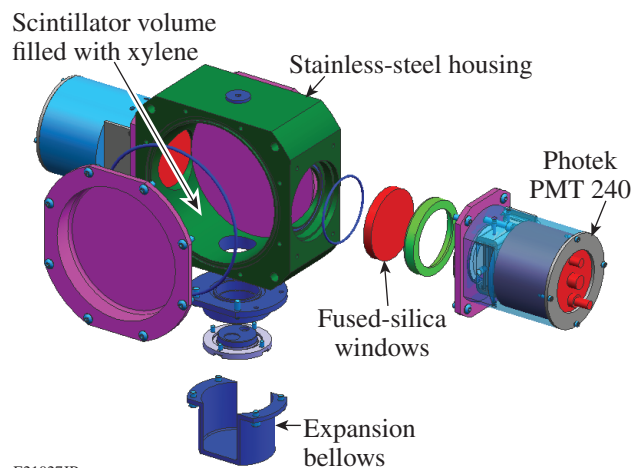
The time-of-flight spectrum in Fig. 131.24 illustrate a number of difficulties when trying to measure neutrons over a dynamic range of 10^5 while maintaining sensitivity in the instrument. One issue is the dominant DT peak that accounts for more than 90% of the neutron energy deposited in the detector. Such a large impulse will saturate the photomultiplier tube (PMT) and produce a long light-afterglow component in the scintillator.[13] The lower-energy neutrons in the detector are masked by the afterglow component from the primary peak that is still present from the scintillation process. Another consideration for high-yield DT implosions is the neutron scat-

tering from the target chamber walls and surrounding concrete structures. Three crucial innovations were needed to achieve high-resolution measurements of the neutron energy spectrum.

A gated PMT was used to exclude the primary DT peak from the time-of-flight signal, similar to the detector setup used for fast-ignitor experiments.[13] The microchannel plate (MCP) PMT is gated by applying a positive voltage to the photocathode. The photoelectrons are attracted back toward the photocathode and will not reach the MCP.[19] Once the primary peak has passed, the bias returns to normal and the PMT generates a signal.

Even with the DT peak gated out of the detector, remnants of the scintillation light from the primary DT signal are still evident. To mitigate the long light-afterglow component, advanced scintillating compounds were developed. Oxygenated xylene has been used to reduce the long light-afterglow component by a factor of 10^5 approximately 100 ns after the primary peak.[14]

These modifications led to the construction of a second-generation time-of-flight diagnostic. A computer-aided drawing (CAD) (shown in Fig. 131.25) illustrates the components of the nTOF detector's final design. A significant modification from the first-generation nTOF detector used for the fast-ignitor campaign is a stainless-steel housing lined with gold. The liner is intended to eliminate any possible reaction from the oxygenated xylene that would alter the sensitivity of the detector. The cavity for the nTOF detector is 15 cm in diameter and 5 cm deep. Scintillation

Figure 131.25

A computer-aided design (CAD) of the nTOF detector shows a cavity for the scintillation fluid, the fused-silica windows, and the photomultiplier tube (PMT) mounts. The detector is mounted to the ceiling underneath the Target Bay in a shielded environment to minimize unwanted neutron scattering similar to the setup used in the fast-ignitor experiment.

light from the incident neutrons is viewed through fused-silica windows where the light is coupled to two 40-mm-diam PMT's.

The instrument must be positioned close enough to target chamber center to achieve high neutron statistics but far enough away to interpret the individual components of the energy spectrum. On OMEGA, the maximum distance available for time-of-flight experiments is 13.4 m from the target chamber center. The final necessary modification was to improve the collimation along the line of sight. A Monte Carlo code (MCNP)[20] is used to model the relevant structures in the OMEGA Target Bay and the area underneath the Target Bay. MCNP, developed by the Los Alamos Monte Carlo Group, is used extensively in the nuclear community. This code was cross checked with Geant4 to ensure that the neutron cross sections were in agreement.[21] The simulations showed that the signal to background can be improved by the introduction of a mid-beam collimator. A diagram of the current nTOF detector and mid-beam collimator is shown in Fig. 131.26. The mid-beam collimator has a 60-cm-sq cross section and is ~70 cm in length. It is constructed from high-density polyethylene with a density of ~0.95 g/cm^3. It is mounted on a stand located in the OMEGA Target Bay with semi-permanent mounts. Comparison of data from experiments with and without the mid-beam collimator shows an increase in signal to background by a factor of 2, as shown in Fig. 131.27.

It was determined that a part of the large background was a result of the primary DT neutrons scattering off the target chamber walls. The mid-beam collimator reduced the field of view as seen by the nTOF from the target chamber to provide

Figure 131.27
Simulations identify the large background resulting from the primary DT neutrons scattering from the target chamber. The models in MCNP included a simulation with (red) and without (blue) a mid-beam collimator. These results were then compared with experimental results (black symbols). The signal to background was in good agreement between simulations and data.

an improved signal to background used to measure the DD and backscattered neutron spectra. A second collimator has been considered for placement inside the target chamber to further reduce neutron scattering from the structures (diagnostics) surrounding the cryogenic target. This will be modeled in MCNP to simulate the effects of this additional collimation needed to further improve the signal to background.

The signals from the PMT's are recorded by a 1-GHz Tektronix DPO-7104 digital oscilloscope. Measurements from recent cryogenic DT experiments are shown in Fig. 131.28. The combination of a gated PMT, an advanced scintillation fluid, and the mid-beam collimator in the clear line of sight made it possible to measure a high-resolution neutron spectrum with good signal to background. The DT peak at ~260 ns is suppressed by the gate. A check of the influence of the gating of PMT's on the nTOF signal was performed by adjusting the timing offset of the gate signals on two nominally identical PMT's. The time-of-flight spectrum indicates that after 50 ns the PMT's are fully recovered.

ρR Measurements Using BackScattered Neutron Yields

The nTOF detector must be calibrated before each use on cryogenic DT campaigns since there is evidence that the scintillating fluid exhibits a depletion of oxygen. A loss of oxygen in the xylene affects the sensitivity of the light-emission process and results in an increased long light-afterglow component. This combination of enhanced sensitivity and longer light decay
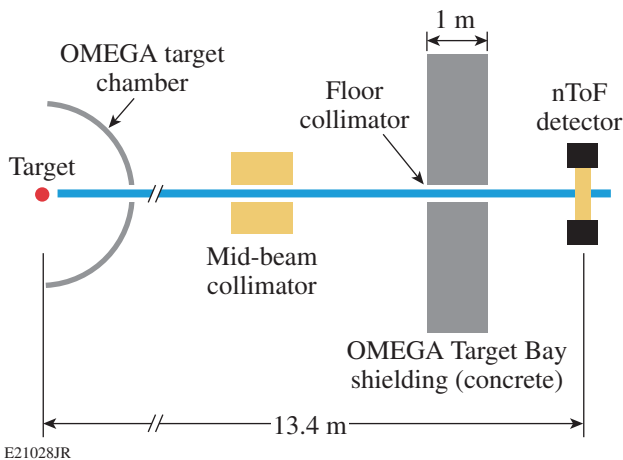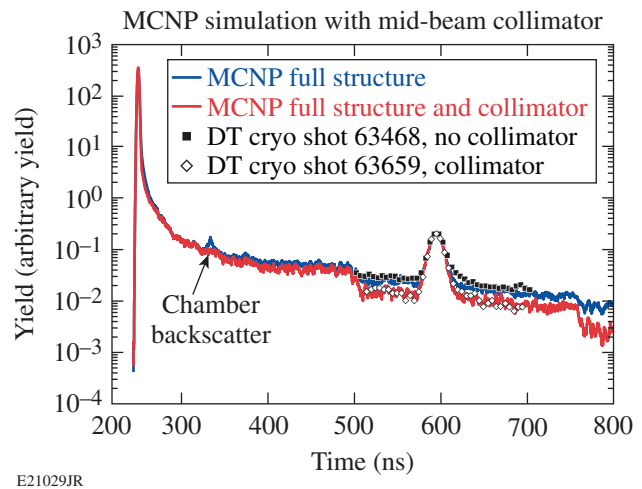

Figure 131.26
A schematic of the target chamber shows the concrete shielding, the nTOF detector's clear line of sight, and the mid-beam collimator. It was determined that the primary DT neutrons scatter off the target chamber walls and produce a large background signal in the nTOF.
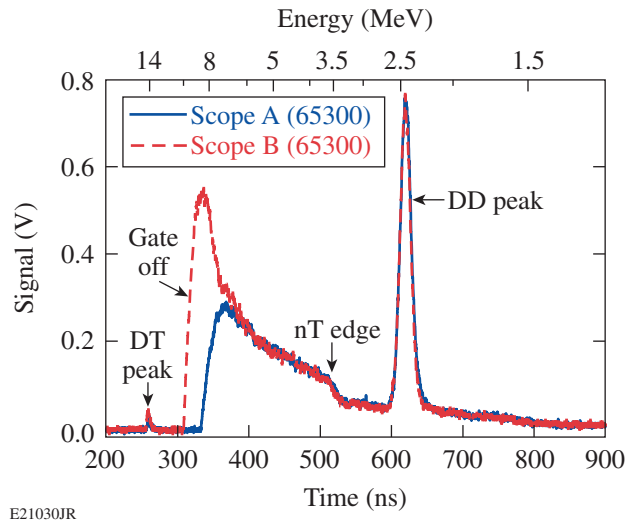
Figure 131.28
To suppress the DT neutron peak, a timing gate is applied to the PMT. The gate recovery has been measured using two PMT 240's, where the time was purposefully offset: PMT A (blue) and PMT B (red). It is clear both PMT's are recovered within 50 ns after the gating is switched off.

will impact the accuracy of the neutron-yield measurement. For this calibration, two D_2-filled targets were imploded with yields that differ by a factor of ~10 to check the linearity of the nTOF detector. A separate detector located in the Target Bay accurately measures the primary neutron yield. Over a six-month period the detector calibration factor changed by ~20%. At this time, it is unclear what causes the xylene to lose the oxygen pressure inside the detector volume.

Recent cryogenic DT implosions have produced neutron yields approaching 1×10^{13} using improved target-positioning procedures and optimized laser pulse shapes on OMEGA.[22] To extract quantitative information from the nTOF signal, the observed spectra are fitted using two of the theoretical components outlined in Fig. 131.24. The first component is the TT spectrum, which is well approximated by a decaying exponential $A \exp(-t/\tau)$ at energies below 6 MeV. The contribution of the TT primary reaction is dependent on the reactivity rate and increases as a function of T_i^4. For this analysis, the overall shape of the spectrum is assumed to be fixed, while the amplitude is scaled from the 1-D simulations where an ion temperature of 2.4 keV was used.

The second component is the down-scattered spectrum that includes both the nT and nD contributions. Since tritium has a half-life of 12.3 years, the fuel D:T ratio changes by ~5% per year. Therefore, it is required to change the nT and nD contributions according to the changing deuterium/tritium fraction

in the DT fuel. This scattered neutron contribution is used to infer the areal density in the nTOF detector. The nT kinematic edge is clearly visible and provides a well-defined region for an accurate fit. An additional background is used to account for the remaining neutron scattering from surrounding structures and remnants of scintillator light decay. The background was found to be quite stable over a number of shots spanning several months. The shape of the background is assumed to be a constant exponential decay, where the amplitude is scaled with the primary DT neutron yield.

This method provides a very good fit to the nTOF spectrum using 1-D simulations as a basis. A number of measurement uncertainties must be considered to obtain an estimate on the accuracy of this analysis. The primary DT neutron yield, needed to adjust the background component, is measured to an accuracy of 5% (Ref. 23). The light output from the scintillator is assumed to be proportional to the energy of the incident neutrons. Given the finite thickness of the scintillator, up to 50% of the incident neutrons pass through the scintillator without any interaction. Since the interaction cross section of neutrons with the scintillator material is a function of the neutron energy, a small correction for the changing interaction probability must be applied to obtain a more-accurate description of the light output. Preliminary simulations of this effect using MCNP with the current xylene nTOF detector indicate that the proportionality assumption introduces an error of ~5%. The best fit to nTOF data is obtained by performing minimization of the error sum to optimize the TT and down-scattered components. The error associated with this method is approximately 2% according to a χ^2 analysis. The high accuracy of this fit is due in part to the large number of neutrons measured by the detector in this region. Below 6 MeV, the nTOF detectors measure above 1×10^5 elastically scattered neutrons (typical on OMEGA cryogenic DT implosions), which introduces a statistical error of ~2%. Errors in the nD and nT elastic scattering cross sections also affect these areal-density measurements. Recent measurements improved the accuracy of the differential nD and nT cross sections, especially at a scattering angle of 180°, to ~10% (Ref. 18). Adding these errors in quadrature gives an estimated total error of ~15%.

However, a number of other error sources have not yet been quantified. The shape of the TT neutron spectrum is not yet well known, which introduces some uncertainty in the fit component. A third theoretical component of the neutron energy spectrum, not included in the fit, is the deuteron breakup reaction D(n,2n)p. This nuclear component will affect the fit primarily in the region below 2 MeV (~700 ns) as seen in Fig. 131.29.
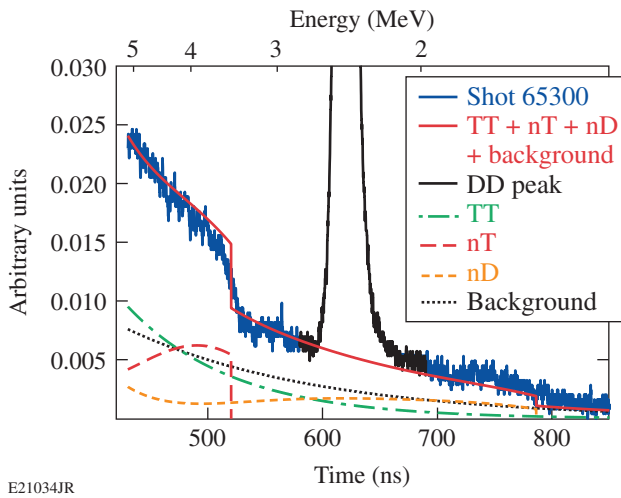
Figure 131.29
Recent nTOF neutron spectra from a DT cryogenic implosion (blue). The DD peak is excluded in this analysis (black). The TT spectrum (green) and the down-scattered component, a combination of the nT and nD spectra (red) are fitted to the experimental data. An additional background component is used that includes any remaining scintillator light decay and neutron scattering (dotted black line). The solid red line illustrates the best fit to this data.

The scattered neutron nTOF diagnostic measured the areal density on a number of recent cryogenic DT implosions on OMEGA. Table 131.V compares the MRS and nTOF data. The comparison between the MRS and nTOF measurements shows

Table 131.V: Predicted ρR obtained from 1-D simulations compared with experimental results from MRS and nTOF. The values from the MRS and nTOF show good agreement. The large ρR difference between nTOF and MRS seen in shots 65578 and 65889 is most likely a result of a target position offset and a misfire on a single beam.

Shot number	1-D prediction (mg/cm^2)	MRS (mg/cm^2)	nTOF (mg/cm^2)
64668	215	163±33	160±32
64669	235	216±30	200±40
65300	210	162±20	160±32
65576	208	155±17	150±30
65578	215	153±15	100±20
65883	190	182±20	160±32
65884	220	126±25	120±24
65887	223	158±21	130±26
65889	216	197±15	140±28

good agreement except for some discrepancies in shots 65578 and 65889. The disagreement in the areal density is most likely a result of the target offset and the misfire of a single laser beam causing significant ρR asymmetry. These asymmetries are possible because the MRS and nTOF probe different regions of the shell's areal density.

Summary

High-resolution neutron time-of-flight spectroscopy has been developed at LLE to measure the areal density of OMEGA cryogenic DT implosions. The time-of-flight spectrum of the elastically scattered neutrons is fitted with theoretical spectral components from well-known nuclear processes to infer the areal density. Increased shielding and collimation have significantly reduced the background in nTOF detectors. Initial results indicate the neutron diagnostics (nTOF's) perform very well and have good agreement with the MRS.

A number of improvements are planned for the scattered neutron nTOF system: A new liquid scintillator nTOF detector housing has been designed with a larger scintillator volume and dual PMT's mounted closer to the scintillation fluid than the current design. An additional collimator installed inside the target chamber is under consideration to further reduce the neutron scattering from inside the target chamber. This will be modeled in MCNP to see how much improvement the additional collimation will provide in the signal to background. The increased scintillator volume and better collimation will potentially allow for higher forward- and backscattered neutron statistics with one detector in a single line of sight. For these measurements one of the two PMT's shown in Fig. 131.25 will be replaced with a less-sensitive PMT-140. This PMT-140 will be used to measure the forward-scattered neutrons close to the primary peak. The remaining PMT-240 will measure the lower-energy backscattered neutron spectrum. Additionally, a joint effort between LLNL and LLE is underway to qualify bibenzyl for use in an nTOF detector. Bibenzyl is a new organic scintillator material that shows significantly reduced light-afterglow decay components. Finally, implosion experiments are planned with pure tritium fill to improve the accuracy of the TT fusion neutron energy spectrum.

REFERENCES

1. V. Yu. Glebov, D. D. Meyerhofer, T. C. Sangster, C. Stoeckl, S. Roberts, C. A. Barrera, J. R. Celeste, C. J. Cerjan, L. S. Dauffy, D. C. Eder, R. L. Griffith, S. W. Haan, B. A. Hammel, S. P. Hatchett, N. Izumi, J. R. Kimbrough, J. A. Koch, O. L. Landen, R. A. Lerche, B. J. MacGowan, M. J. Moran, E. W. Ng, T. W. Phillips, P. M. Song, R. Tommasini, B. K. Young, S. E. Caldwell, G. P. Grim, S. C. Evans, J. M. Mack, T. Sedillo, M. D. Wilke, D. C. Wilson, C. S. Young, D. Casey, J. A. Frenje, C. K. Li, R. D. Petrasso, F. H. Séguin, J. L. Bourgade, L. Disdier, M. Houry, I. Lantuejoul, O. Landoas, G. A. Chandler, G. W. Cooper, R. J. Lepeer, R. E. Olson, C. L. Ruiz, M. A. Sweeney, S. P. Padalino, C. Horsfield, and B. A. Davis, Rev. Sci. Instrum. **77**, 10E715 (2006).

2. C. D. Zhou and R. Betti, Phys. Plasmas **15**, 102707 (2008).

3. T. C. Sangster, R. Betti, R. S. Craxton, J. A. Delettrez, D. H. Edgell, L. M. Elasky, V. Yu. Glebov, V. N. Goncharov, D. R. Harding, D. Jacobs-Perkins, R. Janezic, R. L. Keck, J. P. Knauer, S. J. Loucks, L. D. Lund, F. J. Marshall, R. L. McCrory, P. W. McKenty, D. D. Meyerhofer, P. B. Radha, S. P. Regan, W. Seka, W. T. Shmayda, S. Skupsky, V. A. Smalyuk, J. M. Soures, C. Stoeckl, B. Yaakobi, J. A. Frenje, C. K. Li, R. D. Petrasso, F. H. Séguin, J. D. Moody, J. A. Atherton, B. D. MacGowan, J. D. Kilkenny, T. P. Bernat, and D. S. Montgomery, Phys. Plasmas **14**, 058101 (2007).

4. S. Atzeni and J. Meyer-ter-Vehn, *The Physics of Inertial Fusion: Beam Plasma Interaction, Hydrodynamics, Hot Dense Matter*, International Series of Monographs on Physics (Clarendon Press, Oxford, 2004).

5. R. Betti, P. Y. Chang, B. K. Spears, K. S. Anderson, J. Edwards, M. Fatenejad, J. D. Lindl, R. L. McCrory, R. Nora, and D. Shvarts, Phys. Plasmas **17**, 058102 (2010).

6. S. W. Haan, J. D. Lindl, D. A. Callahan, D. S. Clark, J. D. Salmonson, B. A. Hammel, L. J. Atherton, R. C. Cook, M. J. Edwards, S. Glenzer, A. V. Hamza, S. P. Hatchett, M. C. Herrmann, D. E. Hinkel, D. D. Ho, H. Huang, O. S. Jones, J. Kline, G. Kyrala, O. L. Landen, B. J. MacGowan, M. M. Marinak, D. D. Meyerhofer, J. L. Milovich, K. A. Moreno, E. I. Moses, D. H. Munro, A. Nikroo, R. E. Olson, K. Peterson, S. M. Pollaine, J. E. Ralph, H. F. Robey, B. K. Spears, P. T. Springer, L. J. Suter, C. A. Thomas, R. P. Town, R. Vesey, S. V. Weber, H. L. Wilkens, and D. C Wilson, Phys. Plasmas **18**, 051001 (2011).

7. M. J. Edwards, J. D. Lindl, B. K. Spears, S. V. Weber, L. J. Atherton, D. L. Bleuel, D. K. Bradley, D. A. Callahan, C. J. Cerjan, D. Clark, G. W. Collins, J. E. Fair, R. J. Fortner, S. H. Glenzer, S. W. Haan, B. A. Hammel, A. V. Hamza, S. P. Hatchett, N. Izumi, B. Jacoby, O. S. Jones, J. A. Koch, B. J. Kozioziemski, O. L. Landen, R. Lerche, B. J. MacGowan, A. J. MacKinnon, E. R. Mapoles, M. M. Marinak, M. Moran, E. I. Moses, D. H. Munro, D. H. Schneider, S. M. Sepke, D. A. Shaughnessy, P. T. Springer, R. Tommasini, L. Bernstein, W. Stoeffl, R. Betti, T. R. Boehly, T. C. Sangster, V. Yu. Glebov, P. W. McKenty, S. P. Regan, D. H. Edgell, J. P. Knauer, C. Stoeckl, D. R. Harding, S. Batha, G. Grim, H. W. Herrmann, G. Kyrala, M. Wilke, D. C. Wilson, J. Frenje, R. Petrasso, K. Moreno, H. Huang, K. C. Chen, E. Giraldez, J. D. Kilkenny, M. Mauldin, N. Hein, M. Hoppe, A. Nikroo, and R. J. Leeper, Phys. Plasmas **18**, 051003 (2011).

8. S. Skupsky and S. Kacenjar, J. Appl. Phys. **52**, 2608 (1981).

9. C. K. Li, F. H. Séguin, D. G. Hicks, J. A. Frenje, K. M. Green, S. Kurebayashi, R. D. Petrasso, D. D. Meyerhofer, J. M. Soures, V. Yu.

10. J. A. Frenje, C. K. Li, F. H. Séguin, D. T. Casey, R. D. Petrasso, T. C. Sangster, R. Betti, V. Yu. Glebov, and D. D. Meyerhofer, Phys. Plasmas **16**, 042704 (2009).

11. J. A. Frenje, D. T. Casey, C. K. Li, J. R. Rygg, F. H. Séguin, R. D. Petrasso, V. Yu. Glebov, D. D. Meyerhofer, T. C. Sangster, S. Hatchett, S. Haan, C. Cerjan, O. Landen, M. Moran, P. Song, D. C. Wilson, and R. J. Leeper, Rev. Sci. Instrum. **79**, 10E502 (2008).

12. J. A. Frenje, D. T. Casey, C. K. Li, F. H. Séguin, R. D. Petrasso, V. Yu. Glebov, P. B. Radha, T. C. Sangster, D. D. Meyerhofer, S. P. Hatchett, S. W. Haan, C. J. Cerjan, O. L. Landen, K. A. Fletcher, and R. J. Leeper, Phys. Plasmas **17**, 056311 (2010).

13. C. Stoeckl, M. Cruz, V. Yu. Glebov, J. P. Knauer, R. Lauck, K. Marshall, C. Mileham, T. C. Sangster, and W. Theobald, Rev. Sci. Instrum. **81**, 10D302 (2010).

14. R. Lauck *et al.*, IEEE Trans. Nucl. Sci. **56**, 989 (2009).

15. G. F. Knoll, *Radiation Detection and Measurement*, 3rd ed. (Wiley, New York, 2000).

16. J. Delettrez, R. Epstein, M. C. Richardson, P. A. Jaanimagi, and B. L. Henke, Phys. Rev. A **36**, 3926 (1987); P. B. Radha, J. A. Delettrez, R. Epstein, S. Skupsky, J. M. Soures, S. Cremer, and R. D. Petrasso, Bull. Am. Phys. Soc. **44**, 194 (1999).

17. G. R. Caughlan and W. A. Fowler, At. Data Nucl. Data Tables **40**, 283 (1988).

18. J. A. Frenje, C. K. Li, F. H. Séguin, D. T. Casey, R. D. Petrasso, D. P. McNabb, P. Navratil, S. Quaglioni, T. C. Sangster, V. Yu. Glebov, and D. D. Meyerhofer, Phys. Rev. Lett. **107**, 122502 (2011).

19. Photek Ltd., St. Leonards-on-Sea, East Sussex, TN38 9NS, United Kingdom.

20. Los Alamos Monte Carlo Group, "MCNP-A General Monte Carlo N-Particle Transport Code Version 5," Los Alamos National Laboratory Vols. I-III, April, 2003. Available from Radiation Safety Information Computational Center at Oak Ridge National Laboratory as CCC-740.

21. S. Agostinelli *et al.*, Nucl. Instrum. Methods Phys. Res. A 506, 250 (2003).

22. T. C. Sangster, V. N. Goncharov, R. Betti, T. R. Boehly, D. T. Casey, T. J. B. Collins, R. S. Craxton, J. A. Delettrez, D. H. Edgell, R. Epstein, K. A. Fletcher, J. A. Frenje, V. Yu. Glebov, D. R. Harding, S. X. Hu, I. V. Igumenshchev, J. P. Knauer, S. J. Loucks, C. K. Li, J. A. Marozas, F. J. Marshall, R. L. McCrory, P. W. McKenty, D. D. Meyerhofer, P. M. Nilson, S. P. Padalino, R. D. Petrasso, P. B. Radha, S. P. Regan, F. H. Séguin, W. Seka, R. W. Short, D. Shvarts, S. Skupsky, V. A. Smalyuk, J. M. Soures, C. Stoeckl, W. Theobald, and B. Yaakobi, Phys. Plasmas **17**, 056312 (2010).

23. O. Landoas, V. Yu. Glebov, B. Rossé, M. Briat, L. Disdier, T. C. Sangster, T. Duffy, J. G. Marmouget, C. Varignon, X. Ledoux, T. Caillaud, I. Thfoin, and J.-L. Bourgade, Rev. Sci. Instrum. **82**, 073501 (2011).